IEEE Access
Multidisciplinary | Rapid Review | Open Access Journal

Received September 18, 2018, accepted November 7, 2018, date of publication November 13, 2018,
date of current version December 27, 2018.

Digital Object Identifier 10.1109/ACCESS.2018.2881204

Radar Detection and Motion Parameters Estimation of Maneuvering Target Based on the Extended Keystone Transform (July 2018)

JIBIN ZHENG[1], (Member, IEEE), JIANCHENG ZHANG[1], SHUWEN XU[1], (Member, IEEE), HONGWEI LIU[1], (Member, IEEE), AND QING HUO LIU[2], (Fellow, IEEE)

[1]National Laboratory of Radar Signal Processing, Xidian University, Xi'an 710071, China
[2]Department of Electronic Engineering, Duke University, Durham, NC 27708, USA

Corresponding authors: Jibin Zheng (jibin_zheng@sina.cn) and Jiancheng Zhang (zjc7836@126.com)

This work was supported in part by the National Natural Science Foundation of China under Grant 61601341 and Grant 61771367, in part by the Project Funded by the China Postdoctoral Science Foundation under Grant 2015M582615 and Grant 2016T90891, in part by the Young Talent Fund of University Association for Science and Technology in Shaanxi, China, in part by the Program for the National Science Fund for Distinguished Young Scholars under Grant 61525105, in part by the National Natural Science Foundation of Shaanxi Province, Key R&D Program–The Key Industry Innovation Chain of Shaanxi under Grant 2018JM6060, and in part by the 111 Project under Grant B18039.

ABSTRACT This paper focuses on the range migration (RM) and Doppler frequency migration corrections of the long-time coherent integration, and a fast algorithm is proposed for maneuvering target detection and motion parameters estimation under a low signal-to-noise ratio (SNR). By utilizing the autocorrelation function with respect to the slow time, the newly defined extended keystone transform, scaled Fourier transform, and fast Fourier transform (FFT), the proposed algorithm coherently integrates the target energy into a peak in a three-dimensional (3-D) parameter space. Thereafter, the target's radial velocity and acceleration are estimated by the peak's coordinate. After compensating off the RM and DFM via the estimated motion parameters, the inverse FFT along the range frequency and azimuth FFT are used to realize the coherent integration for the target detection. The cross term characteristic is also analyzed and shows the applicability of the proposed algorithm in the scenario of multiple targets. Comparisons with representative algorithms in the computational complexity, motion parameters estimation, and target detection are presented in this paper, which leads us to conclude that the proposed algorithm can greatly reduce the computational complexity with an acceptable integration SNR gain loss. Finally, the experiments with the simulated and real measured radar data are conducted to verify the proposed algorithm.

INDEX TERMS Long-time coherent integration, maneuvering target, range migration, Doppler frequency migration, extended keystone transform.

I. INTRODUCTION

Target detection and motion parameters estimation are main applications of radar, which have received wide attention in the past decades [1]–[3]. The conventional pulse compression and Doppler processing method [1] is usually used, and achieves a good performance under the assumption that the target moves with a constant velocity and stays in the same range cell within the integration time. With the development of science and technology, especially the stealth technology, the target's radar cross section (RCS) becomes lower and lower. In order to improve the signal-to-noise ratio (SNR) without any changes of radar systems, the long-time coherent integration technique [4], [5] is developed. It can significantly improve the radar detection and motion parameters estimation under a low SNR. However, the long-time coherent integration faces two challenges: 1) the target may not remain within the same range cell during a long integration time, i.e., the range migration (RM) happens; 2) the nonlinear motions (i.e., acceleration, jerk, and so on) result in a time-varying Doppler frequency, and when the Doppler frequency change exceeds a Doppler resolution, the Doppler frequency migration (DFM) happens. The RM and DFM make the echo energy smear in the range-Doppler domain [6]. Therefore, the RM and DFM should be compensated for maneuvering

target detection and motion parameters estimation under the long-time coherent integration.

The keystone transform (KT)-based method [7]–[13] and Radon transform (RT)-based method [14]–[18] are typical methods for the RM correction. The KT can blindly correct the linear RM induced by the target's velocity via scaling the slow time with the range frequency [7], [8]. The second-order KT (SKT) [9], [10] is proposed to blindly eliminate the range curvature (quadratic RM induced by the target's acceleration). The Doppler KT [11] and generalized KT [12] are improved versions of the KT, which are developed for specific applications. The current studies of the KT-based method mainly aim to resolve 1) the unknown Doppler ambiguity, and 2) the Doppler spectrum spanning more than one pulse repetition frequency (PRF) band. The RT-based method corrects the RM via the ergodic searching in the motion parameter space. When the target's motion parameters are matched by the searching parameters, the RM would be corrected. The Radon Fourier transform (RFT) [14], generalized RFT (GRFT) [15], Radon fractional Fourier transform (RFrFT) [16], Radon Lv's distribution (RLVD) [17] and Radon-linear canonical ambiguity function [18] all use the RT-based method to correct the RM. The current studies of the RT-based method mainly aim to resolve 1) the blind speed sidelobe (BSSL), and 2) the high computational cost. Aiming at challenges of the KT-based method and RT-based method, the adjacent cross correlation function (ACCF) -based method [19]–[21] is developed. Unfortunately, the ACCF operation has a high demand on the input SNR. The scaled inverse Fourier transform (SIFT)-based method [22] and frequency domain deramp KT -based method [23] can balance the computational cost and anti-noise performance. However, they are only applicable for the target with a constant velocity.

The DFM of the maneuvering target is induced by the high-order motion, i.e., acceleration. According to the Weierstrass approximation principle [16], the echoes of the maneuvering target along the azimuth can be approximated by the linear frequency modulated (LFM) signal. Therefore, the parameter estimation methods for the LFM signal can be used for the DFM compensation [24]–[26]. The SKT-FRFT [27], second-order Wigner-Ville distribution (SoWVD)-based method [13] and improved axis rotation fractional Fourier transform [28] are all based on the parameter estimation methods for the LFM signal. It is noted that, besides the DFM, the acceleration also induces the quadratic RM. Therefore, the quadratic RM and DFM usually need to be considered and compensated simultaneously for the detection and motion parameters estimation, especially in the radar with a large bandwidth. The GRFT, RFrFT and RLVD are based on this kind of principle to compensate the DFM. Unfortunately, these algorithms need the three-dimensional (3-D) ergodic searching.

To correct the RM and DFM with a lower computational complexity, a novel algorithm basing on extended KT (EKT) is proposed for the maneuvering target under a low SNR. This algorithm firstly coherently integrates the target energy into a peak in a 3-D parameter space and completes estimations of the target's radial velocity and acceleration. Thereafter, compensating off the RM and DFM via the estimated motion parameters, we use the inverse FFT (IFFT) along the range frequency and azimuth FFT to realize the coherent integration for the target detection. The computational complexity, motion parameters estimation and target detection performance of the proposed method are analyzed and compared with several typical algorithms. Mathematical conclusions and numerical simulations demonstrate that the proposed algorithm can greatly reduce the computational complexity with an acceptable integration SNR gain loss. The real measured radar data is also conducted to verify the proposed algorithm.

The rest of this paper is organized as follows. The signal model for the accelerating target is built in Section II. In Section III, the proposed algorithm in single target and multiple targets scenarios are discussed separately, and several examples are presented. Section IV analyzes the performances of the proposed algorithm including: the computational complexity, motion parameters estimation and target detection performances, and comparisons are also performed. Some experiments with the simulated and real data are carried out to verify the proposed algorithm in Section V. Finally, we draw the conclusion in Section VI.

II. SIGNAL MODEL FOR MANEUVERING TARGET

Suppose the radar transmits the LFM signal pulse [15], which takes the form

$$s_t(t) = \mathrm{rect}\left(\frac{t}{T_p}\right)\exp\left[j\left(2\pi f_c t + \pi\gamma t^2\right)\right] \tag{1}$$

where t represents the fast time, i.e., the intra-pulse sampling time. $\mathrm{rect}\left(t/T_p\right) = \begin{cases} 1, & |t| \le T_p/2 \\ 0, & |t| > T_p/2 \end{cases}$ is a rectangular pulse with the width $T_p \cdot f_c$ denotes the carrier frequency. $\gamma = B/T_p$ is the frequency modulation rate and B is the signal bandwidth.

Consider a monostatic radar, where the transmitter and receiver are at the same location. Assume that K targets are in the radar field of view. The received signals from K targets can be modeled as

$$S_r(t, t_n) = \sum_{k=1}^{K}\rho_{0k}\mathrm{rect}\left(\frac{t-\tau_k}{T_p}\right) \times \exp\left[j2\pi f_c(t-\tau_k) + j\pi\gamma(t-\tau_k)^2\right] \tag{2}$$

where ρ_{0k} denotes the kth target backscatter coefficient n is the pulse number and t_n represents the slow time i.e., the inter-pulse sampling time. $\tau_k = 2r_k(t_n)/c$ is the time delay of the kth target. c is the speed of the electromagnetic wave and $r_k(t_n)$ denotes the instantaneous slant range between the radar platform and the kth target.

After demodulation with the reference signal $\exp(-j2\pi f_c t)$, the baseband echoes are of the form

$$\boldsymbol{S}_r(t,t_n)=\sum_{k=1}^{K}\rho_{0k}\mathrm{rect}\left[\frac{t-2r_k(t_n)/c}{T_p}\right]\times\exp\left\{-j2\pi\frac{2r_k(t_n)}{\lambda}+j\pi\gamma\left[t-\frac{2r_k(t_n)}{c}\right]^2\right\}\quad(3)$$

where $\lambda=c/f_c$ denotes the wavelength.

Performing the pulse compression, we get

$$\boldsymbol{S}_c(t,t_n)=\sum_{k=1}^{K}\rho_{ck}\mathrm{sinc}\times\left\{B\left[t-\frac{2r_k(t_n)}{c}\right]\right\}\exp\left[-j2\pi\frac{2r_k(t_n)}{\lambda}\right]\quad(4)$$

where ρ_{ck} denotes the kth target amplitude after the pulse compression $\mathrm{sinc}(x)=\sin(\pi x)/\pi x$ denotes the sinc function.

According to the Weierstrass approximation principle [16], $r_k(t_n)$ can be approximated by a polynomial function with respect to the slow time within a finite coherent time. Neglecting the higher order motions than acceleration, $r_k(t_n)$ can be given as

$$r_k(t_n)=r_k+v_k t_n+a_k t_n^2/2\quad(5)$$

where r_k,v_k, and a_k denote the kth target's initial range, radial velocity and acceleration, respectively.

Substituting (5) into (4), we have

$$\boldsymbol{S}_c(t,t_n)=\sum_{k=1}^{K}\rho_{ck}\mathrm{sinc}\left\{B\left[t-\frac{2\left(r_k+v_k t_n+a_k t_n^2/2\right)}{c}\right]\right\}\times\exp\left[-j2\pi\frac{2\left(r_k+v_k t_n+a_k t_n^2/2\right)}{\lambda}\right]\quad(6)$$

For the high-speed target, the Doppler ambiguity may occur [14], [16], and therefore, the radial velocity of the kth target can be rewritten as

$$v_k=M_k v_{am}+v_{0k}\quad(7)$$

where M_k denotes the kth target's Doppler ambiguity integer $v_{am}=\lambda\cdot PRF/2$ is the blind speed. v_{0k} denotes the kth target's ambiguous velocity.

Upon inserting $\exp\left(-j4\pi M_k v_{am}t_n/\lambda\right)=1$ and (7) into (6), the echoes become

$$\boldsymbol{S}_c(t,t_n)=\sum_{k=1}^{K}\rho_{ck}\mathrm{sinc}\left\{B\left[t-\frac{2\left(r_k+v_k t_n+a_k t_n^2/2\right)}{c}\right]\right\}\times\exp\left(-j4\pi\frac{v_{0k}t_n}{\lambda}\right)\times\exp\left(-j4\pi f_c\frac{r_k+a_k t_n^2/2}{c}\right)\quad(8)$$

As shown in (8), the phase and envelop of the transmitting signal are both modulated by the target's motions. The sinc function of (8) indicates that the target's motions lead to the envelope shift (i.e., RM). Although the Doppler frequency induced by the target's radial velocity is constant, the target's radial acceleration causes a linearly time-varying Doppler frequency (i.e., linear DFM) as shown in the second exponential term of (8). Therefore, to guarantee the coherent integration, the RM and DFM corrections must be done.

III. MANEUVERING TARGET DETECTION AND MOTION PARAMETERS ESTIMATION VIA THE PROPOSED METHOD

In what follows, a novel method is proposed for maneuvering target detection and motion parameters estimation, which can correct the RM and DFM, and realize the coherent integration Taking the Fourier transform (FT) of (8) with respect to the fast time yields

$$\boldsymbol{S}(f_r,t_n)=\sum_{k=1}^{K}\rho_k\ \mathrm{rect}\left(\frac{f_r}{B}\right)\exp\left(-j4\pi\frac{v_{0k}t_n}{\lambda}\right)\times\exp\left(-j4\pi f_r\frac{v_k t_n}{c}\right)\times\exp\left[-j4\pi\left(f_c+f_r\right)\frac{r_k+a_k t_n^2/2}{c}\right]\quad(9)$$

where $\rho_{ck}\approx B\rho_k.f_r$ is the range frequency.

A. SINGLE TARGET

For clarity, we first consider a single target in the scenario. According to (9), the kth target's echoes in the range frequency and slow time domain take the form.

$$\boldsymbol{S}_k(f_r,t_n)=\rho_k\ \mathrm{rect}\left(\frac{f_r}{B}\right)\exp\left(-j4\pi\frac{v_{0k}t_n}{\lambda}\right)\times\exp\left(-j4\pi f_r\frac{v_k t_n}{c}\right)\times\exp\left[-j2\pi\left(1+\frac{f_r}{f_c}\right)\frac{2r_k+a_k t_n^2}{\lambda}\right]\quad(10)$$

To estimate the target's radial velocity and acceleration, we firstly define a bilinear autocorrelation function

$$\boldsymbol{R}_k(f_r,t_n,\tau_n)=AF_{t_n}\left[S_k(f_r,t_n)\right]=S_k(f_r,t_n+\tau_n)\,S_k^{\dagger}(f_r,t_n-\tau_n)\quad(11)$$

where τ_n denotes the lag time variable with respect to the slow time $AF_{t_n}[\cdot]$ denotes the autocorrelation along the t_n axis. The superscript † represents the complex conjugation.

Upon substituting (10) into (11), the auto term of the kth target can be expressed as

$$\boldsymbol{R}_k(f_r,t_n,\tau_n)=\rho_k^2\mathrm{rect}\left(\frac{f_r}{B}\right)\exp\left(-j8\pi\frac{v_{0k}\tau_n}{\lambda}\right)\times\exp\left(-j8\pi f_r\frac{v_k\tau_n}{c}\right)\times\exp\left[-j8\pi\left(1+\frac{f_r}{f_c}\right)\frac{a_k\tau_n t_n}{\lambda}\right]\quad(12)$$

The observation of (12) shows that the third exponential term includes the coupling among the range frequency f_r, slow time t_n, and lag time τ_n. If we directly perform the FT on (12) with regard to t_n, we would get

$$\begin{aligned}\boldsymbol{U}'_k(f_r,f_d,\tau_n) &= FT_{t_n}[\boldsymbol{R}_k(f_r,t_n,\tau_n)]\\ &= \rho_{1k}\mathrm{rect}\left(\frac{f_r}{B}\right)\exp\left(-j8\pi\frac{v_{0k}\tau_n}{\lambda}\right)\\ &\quad\times\exp\left(-j8\pi f_r\frac{v_k\tau_n}{c}\right)\delta\\ &\quad\times\left[f_d+\frac{4\left(1+f_r/f_c\right)a_k\tau_n}{\lambda}\right] \end{aligned} \tag{13}$$

where f_d denotes the Doppler frequency with respect to t_n, and $FT_{t_n}[\cdot]$ denotes the FT operation along the t_n axis.

As can be seen from (13), since the FT operation cannot decouple the coupling among f_r, t_n, and τ_n, the target energy has been accumulated into the quadratic surface $f_d = -4\left(1+f_r/f_c\right)a_k\tau_n/\lambda$ in the 3-D space. Clearly, it does not benefit the further energy integration.

To eliminate the coupling between the range frequency and slow time, the well-known KT rescales the slow time axis in accordance with $t_m = \left(1+f_r/f_c\right)t_n$. In [29], the scaled Fourier transform (SFT) is proposed to remove the coupling between τ_n and t_n by performing the scaling $t_m = \tau_n t_n$. However, if we perform the KT on (12), the coupling between the slow time and lag time still left. Accordingly, if we apply the scaling $t_m = \tau_n t_n$ to (12), the new scaled slow time variable t_m and range frequency still couple with each other.

Here, to remove the coupling among these three variables, we borrow ideas of the KT and SFT to propose a novel transform known as the EKT. The scaling formula of EKT takes the form

$$t_m = \xi\left(1+f_r/f_c\right)\tau_n t_n \tag{14}$$

where t_m denotes the scaled slow time variable. ξ is a zoom factor, which is introduced to adjust the acceleration estimation range. Note that the selection criterion of the zoom factor should combine the estimation accuracy with the estimation range. Usually, we base specific applications to set the zoom factor [32].

Now, performing the EKT on (12), i.e., rescaling the slow time variable based on (14), we have

$$\begin{aligned}\boldsymbol{P}_k(f_r,t_m,\tau_n) &= \rho_k^2\mathrm{rect}\left(\frac{f_r}{B}\right)\exp\left(-j8\pi\frac{v_{0k}\tau_n}{\lambda}\right)\\ &\quad\times\exp\left(-j8\pi f_r\frac{v_k\tau_n}{c}\right)\exp\left(-j8\pi\frac{a_k t_m}{\lambda\xi}\right)\end{aligned} \tag{15}$$

By comparing the third exponential term of (15) with that of (12), we observe that the coupling has been removed by the EKT operation. Thereafter, taking the FT of (15) along the scaled slow time axis, we obtain

$$\begin{aligned}\boldsymbol{U}_k(f_r,f_{sd},\tau_n) &= FT_{t_m}[\boldsymbol{P}_k(f_r,t_m,\tau_n)]\\ &= \rho_{1k}\mathrm{rect}\left(\frac{f_r}{B}\right)\exp\left(-j8\pi\frac{v_{0k}\tau_n}{\lambda}\right)\\ &\quad\times\exp\left(-j8\pi f_r\frac{v_k\tau_n}{c}\right)\delta\left(f_{sd}+\frac{4a_k}{\lambda\xi}\right)\end{aligned} \tag{16}$$

where f_{sd} denotes the Doppler frequency with respect to t_m. The observation of (16) shows that the target energy has been integrated into the plane $f_{sd} = -4a_k/(\lambda\xi)$ in the 3-D space. Therefore, the remaining operations are devoted to realizing the energy accumulation along other two dimensions.

The coupling between the range frequency and lag time variable in the second exponential term of (16) still influences the energy integration. If we perform the inverse FT (IFT) on (16) with respect to f_r, it would yield

$$\begin{aligned}\boldsymbol{V}'_k(t,f_{sd},\tau_n) &= IFT_{f_r}[\boldsymbol{U}_k(f_r,f_{sd},\tau_n)]\\ &= \rho_{2k}\mathrm{sinc}\left[B\left(t-\frac{4v_k}{c}\tau_n\right)\right]\\ &\quad\times\exp\left(-j8\pi\frac{v_{0k}\tau_n}{\lambda}\right)\delta\left(f_{sd}+\frac{4a_k}{\lambda\xi}\right)\end{aligned} \tag{17}$$

where $IFT_{f_r}[\cdot]$ denotes the IFT operation along the f_r axis.

As can be seen from (17), the target energy peaks along an inclined line $t = 4v_k\tau_n/c$ in the cross section of $\boldsymbol{V}'_k(t,f_{sd},\tau_n)$ for $f_{sd}+4a_k/(\lambda\xi)=0$. Therefore, the direct FT on (17) with respect to τ_n cannot realize the energy integration in the lag time dimension. In (18), we apply the SIFT [22] to eliminate the coupling between the range frequency and lag time in the second exponential term of (16).

$$\begin{aligned}\boldsymbol{V}_k(t_s,f_{sd},\tau_n) &= \int_{f_r}\boldsymbol{U}_k(f_r,f_{sd},\tau_n)\exp(j2\pi\zeta t_s\tau_n f_r)\,df_r\\ &= \rho_{2k}\mathrm{sinc}\left[B\left(t_s-\frac{4v_k}{\zeta c}\right)\right]\\ &\quad\times\exp\left(-j8\pi\frac{v_{0k}\tau_n}{\lambda}\right)\delta\left(f_{sd}+\frac{4a_k}{\lambda\xi}\right)\end{aligned} \tag{18}$$

where t_s denotes the scaled fast time. ζ is a zoom factor, which is introduced to adjust the velocity estimation range.

In (18), the target energy has been integrated into the intersection of two planes [$f_{sd} = -4a_k/(\lambda\xi)$ and $t_s = 4v_k/(\zeta c)$] in the 3-D space. Thereafter, we can apply the FT to accomplish the energy integration.

$$\begin{aligned}&\boldsymbol{Z}_k\left(t_s,f_{sd},f_{pd}\right)\\ &= FFT_{\tau_n}[\boldsymbol{V}_k(t_s,f_{sd},\tau_n)]\\ &= \rho_{3k}\mathrm{sinc}\left[B\left(t_s-\frac{4v_k}{\zeta c}\right)\right]\delta\left(f_{sd}+\frac{4a_k}{\lambda\xi}\right)\delta\left(f_{pd}+\frac{4v_{0k}}{\lambda}\right)\end{aligned} \tag{19}$$

where f_{pd} represents the pseudo Doppler frequency with respect to τ_n.

In (19), we have accomplished the coherent target energy integration along the slow time, range frequency and lag time

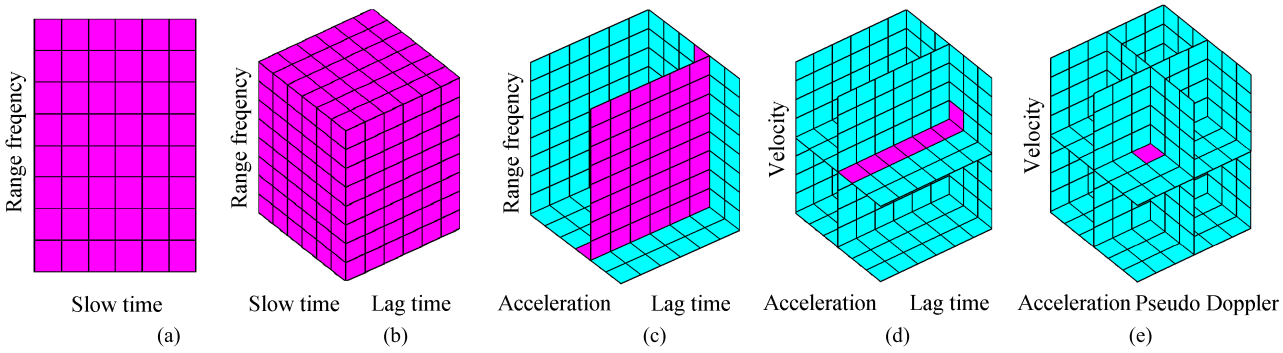

FIGURE 1. Target energy distribution at different processing stages. (a) Target energy distribution in the range frequency and slow time domain. (b) Target energy distribution after the slow time correlation. (c) Target energy distribution after the EKT and FT operations. (d) Target energy distribution after the SIFT operation with respect to the range frequency. (e) Target energy distribution after performing the FT along the lag time axis.

axes via the EKT, SIFT and FT operations. The target energy peaks at the point $\left[4v_k/(\zeta c), -4a_k/(\lambda\xi), -4v_{0k}/\lambda\right]$ in the 3-D space. Via the peak detection, the kth target's radial velocity and acceleration can be estimated as

$$\hat{v}_k = \zeta c t_s/4 \tag{20}$$

$$\hat{a}_k = -\lambda\xi f_{sd}/4 \tag{21}$$

The above procedures can be summarized as

$$\begin{aligned}&\boldsymbol{Z}\left(t_s, f_{sd}, f_{pd}\right)\\ &= FT_{\tau_n}\left\{SIFT_{f_r}\left\{FT_{t_m}\left[EKT_{t_n}\left[AF_{t_n}\left(\boldsymbol{S}\left(f_r, t_n\right)\right)\right]\right]\right\}\right\}\end{aligned} \tag{22}$$

Note that variables in (22) have been indicated above and readers can refer to (10)-(19). The target energy distribution at aforementioned processing stages can be qualitatively described by FIGURE. 1. FIGURE. 1(a) shows the target energy distribution in the range frequency and slow time domain [Eq. (10)]. By performing the autocorrelation function defined in (11), the target energy spreads into a 3-D space (range frequency, slow time, and lag time), as shown in FIGURE. 1(b). FIGURE. 1(c) shows that the target energy has been integrated into a plane after the EKT and FT operations. Thereafter, by performing the SIFT with respect to the range frequency in FIGURE. 1(c), the target energy is integrated into a line in FIGURE. 1(d). Finally, via the FT operation along the lag time in FIGURE. 1(d), the target energy is successively integrated into a point in the 3-D space, as shown in FIGURE. 1(e).

With estimated motion parameters in (20) and (21), we construct a compensations function as follows:

$$\begin{aligned}\boldsymbol{Y}\left(f_r, t_n; \hat{v}_k, \hat{a}_k\right) &= \exp\left(j4\pi f_r \frac{\hat{v}_k t_n}{c}\right)\\ &\times \exp\left[j4\pi\left(f_c + f_r\right)\frac{\hat{a}_k t_n^2/2}{c}\right].\end{aligned} \tag{23}$$

In (23), the first exponential term can compensate the RM induced by the target's radial velocity, and the second exponential term can compensate the quadratic RM and DFM induced by the target's radial acceleration. By multiplying (23) with (10), the RM and DFM of the kth target will be compensated simultaneously. Then, the coherent integration can be realized by using the range frequency IFT and azimuth FT as follows:

$$\begin{aligned}&\boldsymbol{S}_1\left(t, f_d\right)\\ &= FT_{t_n}\left\{IFT_{f_r}\left[\boldsymbol{Y}\left(f_r, t_n; \hat{v}_k, \hat{a}_k\right)\boldsymbol{S}_k\left(f_r, t_n\right)\right]\right\}\\ &= \rho_{4k}\,\mathrm{sinc}\left[B\left(t - \frac{2r_k}{c}\right)\right]\delta\left(f_d + \frac{2v_{0k}}{\lambda}\right)\exp\left(-\frac{j4\pi r_k}{\lambda}\right)\end{aligned} \tag{24}$$

where ρ_{4k} is the amplitude after the coherent integration. Finally, the constant false alarm rate (CFAR) detection technique [1] is employed to accomplish target detection.

An example is presented below to intuitively explain the proposed method.

Example 1: Consider a single target locating at the 140*th* range cell. Its radial velocity and acceleration are 945 m/s and 60 m/s ^{2}, respectively. The radar parameters are listed in Table 1. The zoom factors ζ and ξ are set as 2 and 4, respectively. According to radar parameters and zoom factors, estimation precisions of the radial velocity and acceleration are 15 m/s and 0.3 m/s^2, respectively. Simulation results are shown in FIGURE. 2.

TABLE 1. Radar parameters.

Parameter	Value	Parameter	Value
Carrier frequency	1 GHz	Pulse width	80 μs
Bandwidth	10 MHz	PRF	512
Sample frequency	10 MHz	Integration pulses	512

The cross section of $\boldsymbol{U}'\left(f_r, f_d, \tau_n\right)$ in (13) for $f_r = 5$ MHz is shown in FIGURE. 2(a), where the target energy peaks along the inclined line $f_d = -800\ \tau_n$. In FIGURE. 2(b), $f_d = -800\tau_n$ in FIGURE. 2(a) is corrected into a beeline $f_{sd} = -200$ Hz due to the EKT operation. FIGURE. 2(c) shows the cross section of $\boldsymbol{V}'\left(t, f_{sd}, \tau_n\right)$ in

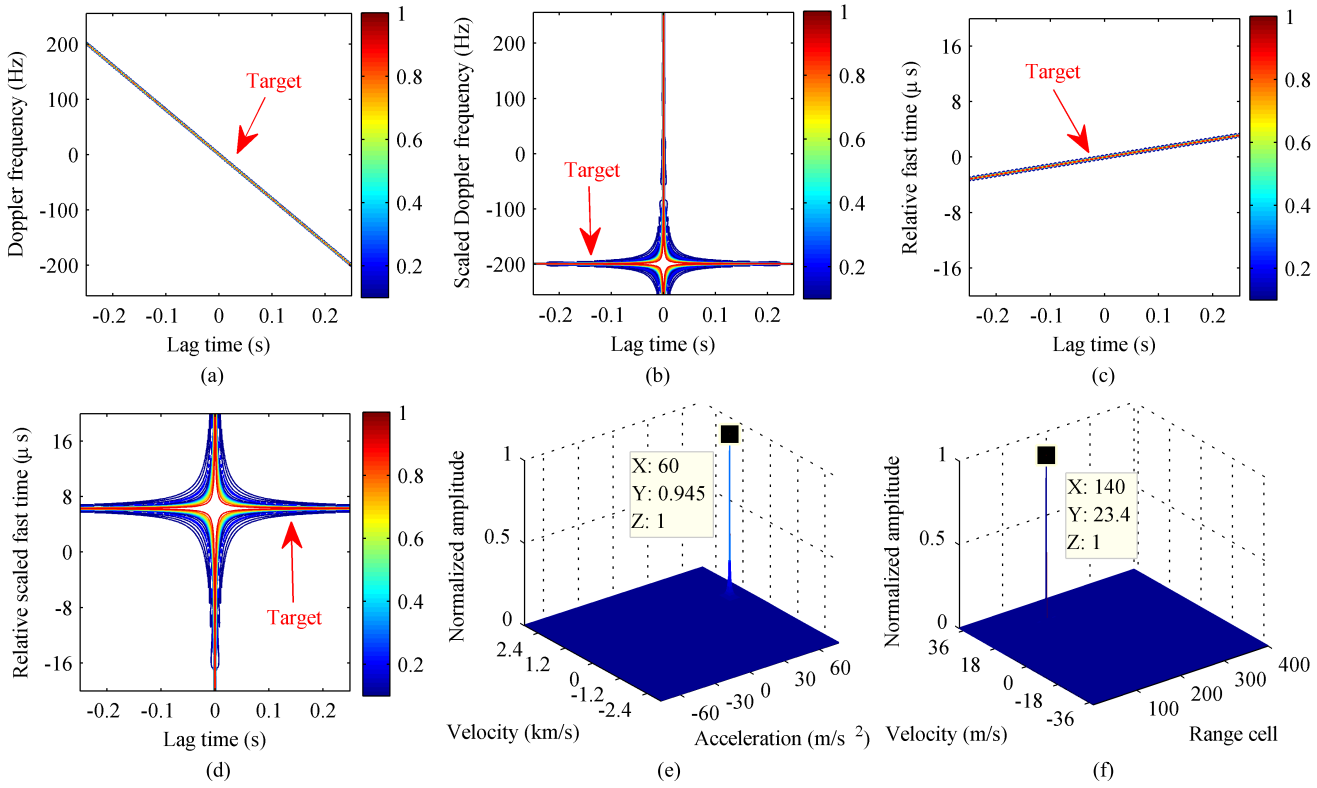

FIGURE 2. Simulation results of *Example 1*. (a) Cross section of $\boldsymbol{U}'(f_r, f_d, \tau_n)$ for $f_r = 5$ MHz. (b) Cross section of $\boldsymbol{U}(f_r, f_{sd}, \tau_n)$ for $f_r = 5$ MHz. (c) Cross section of $\boldsymbol{V}'(t, f_{sd}, \tau_n)$ for $f_{sd} = -200$ Hz. (d) Cross section of $\boldsymbol{V}(t_s, f_{sd}, \tau_n)$ for $f_{sd} = -200$ Hz. (e) Cross section of $\boldsymbol{Z}(t_s, f_{sd}, f_{pd})$ for $f_{pd} + 4v_{0k}/\lambda = 0$. (f) Coherent integration result after the RM and DFM compensations.

(17) for $f_{sd} = -200$ Hz. Via the decouple operation SCIFT, the inclined line in FIGURE. 2(c) is corrected into a beeline $t_s = 6.3$ μs in FIGURE. 2(d). And then, by performing the FT on $\boldsymbol{V}(t_s, f_{sd}, \tau_n)$ along the lag time axis, the target energy is integrated into a peak. FIGURE. 2(e) presents the cross section of $\boldsymbol{Z}(t_s, f_{sd}, f_{pd})$ in (19) for $f_{pd} + 4v_{0k}/\lambda = 0$. By using the peak detection technique, the target's radial velocity and acceleration are estimated as 945 m/s and 60 m/s^2, respectively. Finally, we use these two estimations to compensate the RM and DFM, and FIGURE. 3(f) shows the result after the coherent integration.

Up to this point, we have analyzed the proposed coherent detection method in single target scenario. However, the cross term would appear in multiple targets scenario due to the bilinearity of the autocorrelation function defined in (11), which may affect the peak detection. In the following subsection, the cross term will be analyzed.

B. MULTIPLE TARGETS

This subsection analyzes the cross term to illustrate that the proposed algorithm is also applicable in the scenario of multiple targets. The cross term can be expressed as

$$\boldsymbol{Z}_c(t_s, f_{sd}, f_{pd}) = \sum_{x=1}^{K-1} \sum_{y=x+1}^{K} \boldsymbol{Z}_{c,x,y}(t_s, f_{sd}, f_{pd}) \quad (25)$$

TABLE 2. Targets parameters.

Parameter	TA	TB	TC
Amplitude	1	1	1
Range cell number	150th	220th	240th
Radial velocity (m/s)	900	1200	1200
Radial acceleration (m/s2)	45	45	45

where $\boldsymbol{Z}_{c,x,y}(t_s, f_{sd}, f_{pd})$ denotes the cross term generated by the xth and yth targets. K is the number of targets in the scenario.

Without loss of generality, two targets, the xth and yth targets, are considered. The cross term is derived in **Appendix A**, which demonstrates that the cross term cannot be accumulated as the auto term in the proposed algorithm.

In what follows, an example is given to illustrate the cross term suppression of the proposed method.

Example 2: Three targets denoted by T_A, T_B and T_C are considered, and their motion parameters are listed in Table 2. The radar parameters and the zoom factors are the same as those in ***Example 1***. FIGURE. 3 shows the simulation results.

FIGURE. 3(a) shows the cross section of $\boldsymbol{U}(f_r, f_{sd}, \tau_n)$ for f_r =5 MHz. A beeline f_{sd} =−150 Hz and four curves appear in this plane. T_A, T_B and T_C have the same radial acceleration. Thus, three auto terms $\boldsymbol{U}_A$, $\boldsymbol{U}_B$ and $\boldsymbol{U}_C$ peak along the same beeline. T_B and T_C have the same radial velocity.

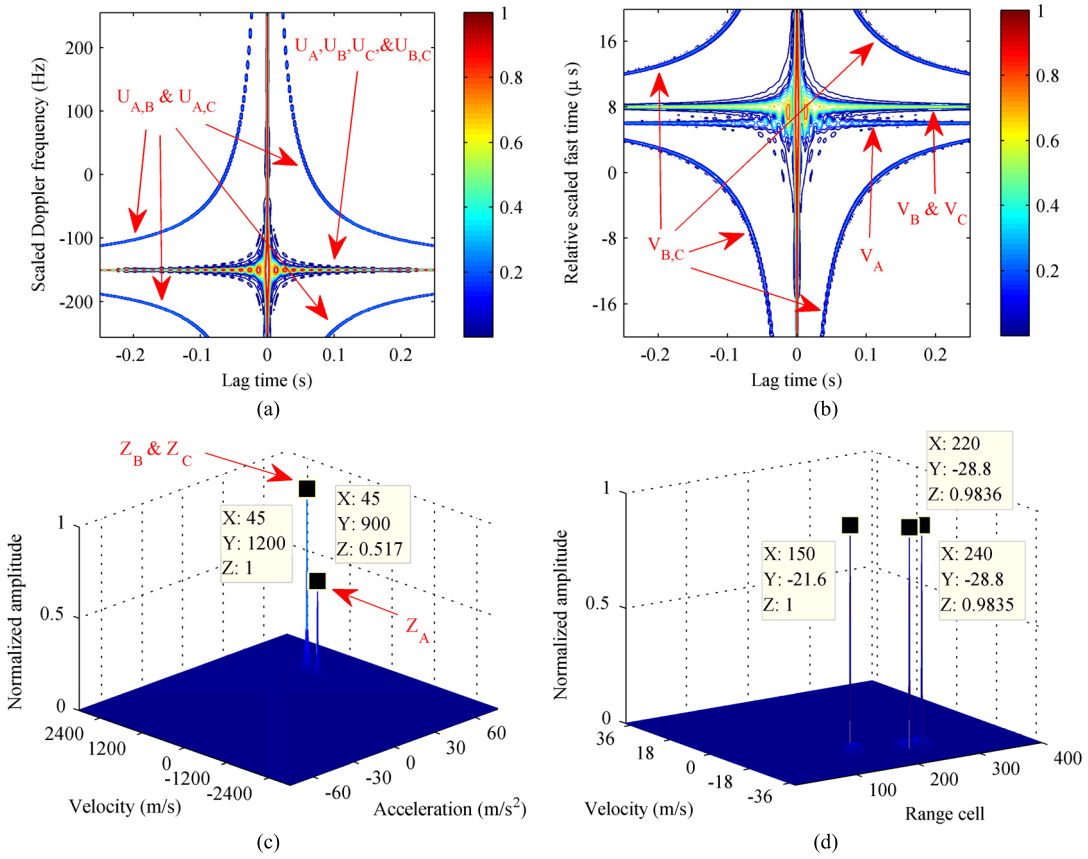

FIGURE 3. Simulation results of E*xample 2*. (a) Cross section of $\boldsymbol{U}(f_r, f_{sd}, \tau_n)$ for f_r =5 MHz. (b) Cross section of $\boldsymbol{V}(t_s, f_{sd}, \tau_n)$ for f_{sd} = -150 Hz. (c) Velocity and acceleration distribution. (d) Coherent integration result after the RM and DFM compensations.

According to (53) in **Appendix B**, the cross term $\boldsymbol{U}_{B,C}$ also peaks along the beeline $f_{sd} = -150$ Hz. Moreover, according to (52) in **Appendix B**, $\boldsymbol{U}_{A,B}$ and $\boldsymbol{U}_{A,C}$ peaks along the same curves. Clearly, $\boldsymbol{U}_{A,B}$ and $\boldsymbol{U}_{A,C}$ could not be further accumulated.

FIGURE. 3(b) shows the cross section of $\boldsymbol{V}(t_s, f_{sd}, \tau_n)$ for $f_{sd} = -150$ Hz. Two beelines $t_s = 6$ μs and $t_s = 8$ μs appear in this plane. With the targets' radial velocity listed in Table 2, we can also calculate $4v_A/(\zeta c) = 6 \times 10^{-6}$ and $4v_B/(\zeta c) = 4v_C/(\zeta c) = 8 \times 10^{-6}$. Moreover, four curves correspond to the cross terms generated by T_B and T_C appear in this cross section, which meets the analysis result in (56) in **Appendix B**

FIGURE. 3(c) presents the cross section of the integration result $\boldsymbol{Z}(t_s, f_{sd}, f_{pd})$ for $f_{pd} + 4v_{0k}/\lambda = 0$. Two pairs of motion parameters (velocity: 900m/s, acceleration: 45 m/s^2) and (1200 m/s, 45 m/s^2) can be estimated via the peak detection. Finally, the coherent integration can be achieved after the RM and DFM compensations with estimated parameters, as shown in FIGURE. 3(d). T_B and T_C are separated in the range domain due to their different locations. It is worthwhile noting that, if targets have different amplitudes (strong and weak targets), the auto term of the weak target may be submerged. Under such a situation, same as other nonlinear methods, we need to employ the CLEAN technique to complete the target detection [31].

The above experimental results conform to the theoretical derivations, which leads us to conclude that the proposed method is also applicable in the scenario of multiple targets.

C. IMPLEMENTATION OF THE PROPOSED METHOD

Based on analyses above, the implementation of the proposed method is summarized in FIGURE. 4, which mainly consists of five steps. The detailed procedures are given as follows. Note that, here, we use the FFT and IFFT to separately speed up the FT and IFT for the fast implementation of the proposed method.

Step 1: Apply the down conversion, pulse compression, and range FFT to the radar raw data.

Step 2: Calculate the bilinear autocorrelation function, and then, employ the EKT, SIFT and FFT to realize coherent energy integration.

Step 3: Conduct the peak detection to accomplish the target's radial velocity and acceleration estimation.

Step 4: Construct a compensation function to compensate the RM and DFM, and then, perform range frequency IFFT

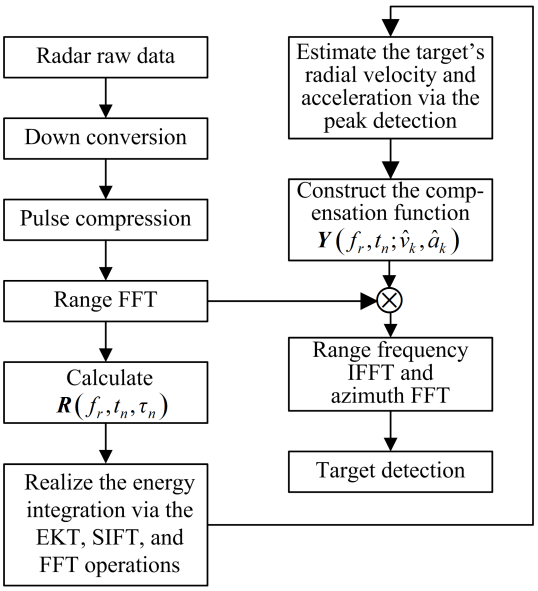

FIGURE 4. Detailed processing steps of the proposed method.

and azimuth FFT to accomplish the coherent integration. Conduct the CFAR detection to realize the target detection.

Step 5: Repeat ***Steps 3-4*** until no target can be detected in **Step 4**.

IV. PERFORMANCE ANALYSIS AND COMPARISONS

In this section, the proposed algorithm is compared with several representative algorithms in terms of computational complexity, motion parameters estimation and target detection performances. The moving target detection (MTD) and RFT cannot work for the maneuvering target due to the RM and DFM. In contrast, the proposed algorithm, GRFT and SOWVD can compensate the RM and DFM. Compared to the MTD and RFT, these three algorithms have obvious advantages for the maneuvering target detection. Therefore, here, we mainly compare the proposed algorithm with the GRFT and SOWVD.

A. COMPUTATIONAL COMPLEXITY

Assume there are M range cells and N integration pulses in the processing data. The searching times of the Doppler ambiguity integer and acceleration are N_{am} and N_a, respectively.

The main steps of the proposed method include: the autocorrelation function defined in (12) [with the computational cost of $O(M^2N)$], the EKT, SIFT and FFT operations performed on $\boldsymbol{R}(f_r, t_n, \tau_n)$ [with the computational cost of $O(MN^2(\log_2 N+\log_2 M))$(the EKT and SIFT can be realized by the chirp-z transform)], and the range frequency IFFT and azimuth FFT operations to realize the coherent integration $[O(MN(\log_2 N + \log_2 M))]$. Therefore, the overall computational complexity of the proposed method is in the order of $O[MN^2(\log_2 N + \log_2 M)]$.

The GRFT compensates the RM and DFM via 3-D searching of the initial range, radial velocity and acceleration. For each searching grid, the computational complexity is in the order of $O(N)$. Since the searching interval of the radial velocity is the Doppler resolution, the searching times of the radial velocity are $N_{am}N$. Therefore, the computational complexity of the GRFT is in the order of $O(N_{am}N_aMN^2)$.

As for the SOWVD-based method, it first corrects the RM via the KT and Doppler ambiguity integer searching, and then employs the SOWVD to realize the DFM compensation. The computational complexity of the SOWVD is in the order of $O(N^2\log_2 N)$ and the SOWVD-based method needs to repeat the SOWVD operation $N_{am}M$ times. Therefore, the computational complexity of the SOWVD-based method is in the order of $O(N_{am}N^2M\log_2 N)$.

TABLE 3. Computational complexity.

Methods	Computational cost
Proposed method	$O[MN^2(\log_2 M+\log_2 N)]$
GRFT	$O(N_{am}N_aN^2M)$
SOWVD-based method	$O(N_{am}N^2M\log_2 N)$

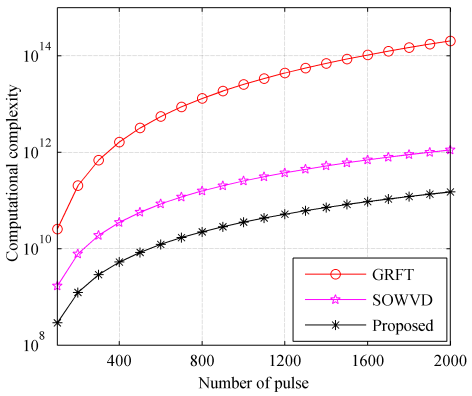

FIGURE 5. Computational complexities of the GRFT, SOWVD-based method and proposed method versus integration pulses.

The computational complexities of these three methods are summarized in Table 3. Assume that the scope of target's velocity is [−2000 m/s, 2000 m/s], $N_a = N$ and $M = 500$. Under different integration pulses (the other radar parameters are the same as those in Table 1), FIGURE. 5 shows computational complexities of these three algorithms.

As shown in Table 3 and FIGURE. 5, the proposed method has the lowest computational complexity among these three methods. The GRFT has the highest computational complexity due to the 3-D searching of the range, velocity and acceleration. If we have some prior knowledge of target's motion parameters, the searching scope may be reduced and the computational complexity of the GRFT may become lower. The KT transform guarantees the higher efficiency of the SOWVD-based method compared with the GRFT.

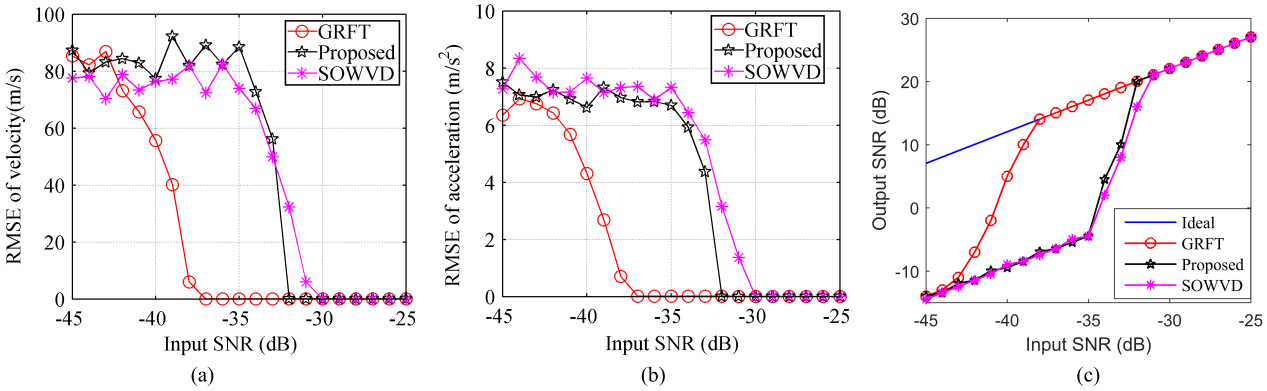

FIGURE 6. RMSE of the estimated motion parameters and the input-output SNR performance. (a) RMSE of the estimated velocity. (b) RMSE of the estimated acceleration. (c) Input-output SNR performances.

However, it still has a higher computational cost than the proposed method.

B. MOTION PARAMETERS ESTIMATION PERFORMANCE

The estimation accuracies of target's radial velocity and acceleration affect the RM and DFM compensations, and further impact the target detection. In this subsection, the motion parameters estimation performance of the proposed method is analyzed.

The radar parameters are set as follows: carrier frequency f_c =1 GHz, pulse width T_p =80 μs, bandwidth B=5 MHz, sample frequency f_s =5 MHz and PRF =200 Hz. 400 effective pulses are used. The complex white Gaussian noise is added to the echoes and the input SNRs are [−45 dB: 1 dB:−25 dB]. 200 times Monte Carlo trials are done for each input SNR value. For convenience, a single target locating at the 90th range cell is considered. Its radial velocity and acceleration are 750 m/s and 12 m/s^2, respectively.

FIGUREs. 6 (a) and (b) shows the root mean square errors (RMSEs) of the estimated target's radial velocity and acceleration of the proposed method, GRFT, and the SOWVD-based method. The RMSE is defined as $\sigma_x = \sqrt{\sum_{i=1}^{100}\left(\hat{x}_i - x_i\right)^2 \Big/ 100}$, where $\hat{x}_i$ denotes the estimated value of the real value x_i in the ith Monte Carlo trial. The input-output SNR performances [6] of these three methods are also shown in FIGURE. 6(c), where the ideal input-output SNR is also shown for reference.

The GRFT is linear and uses the 3-D searching to realize the coherent integration. As seen from FIGURE. 6, the GRFT has the best RMSE versus input SNR. The proposed method is based on a bilinear kernel function and suffers from about 6 dB SNR loss compared to the GRFT. The SOWVD-based method has the worst RMSE versus input SNR. This is because it is based on a fourth-order kernel function.

C. DETECTION PERFORMANCE

In this subsection, we employ the CFAR detection technique to evaluate the target detection performance of the proposed method. The radar parameters and target's motion parameters are the same as those in Subsection IV-B. The input SNRs are [−45 dB:1 dB:−10 dB] and 200 times Monte Carlo trials are conducted for each input SNR value. FIGURE. 7 shows the detection probability under the false alarm probability 10^{-6}. The detection performances of GRFT, SOWVD-based method, RFT and MTD are shown for comparison. Note that the RFT and MTD are used to demonstrate obvious advantages of other three methods.

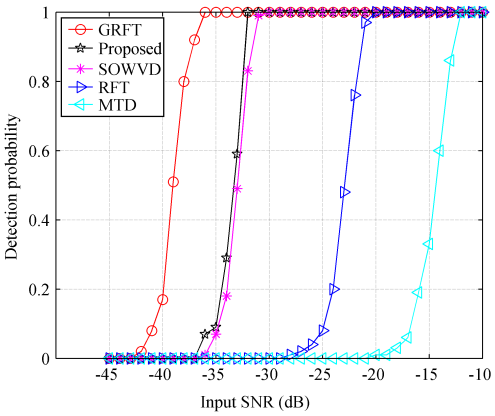

FIGURE 7. Detection probabilities of the GRFT, SOWVD-based method, proposed method, RFT and MTD under different input SNRs.

As seen from FIGURE .7, the detection performance of the proposed algorithm is worse than that of the GRFT, while better than that of the SOWVD-based method. Combining with the computational complexity analysis in Subsection IV-A and motion parameters estimation in Subsection IV-B, we conclude that the proposed algorithm can greatly reduce the computational complexity with an acceptable integration SNR gain loss The RFT cannot remove the RM and DFM induced by the target's radial acceleration, and the MTD has the serious RM and DFM. Therefore, their detection performances are worse than those of other three algorithms, as shown in FIGURE. 7.

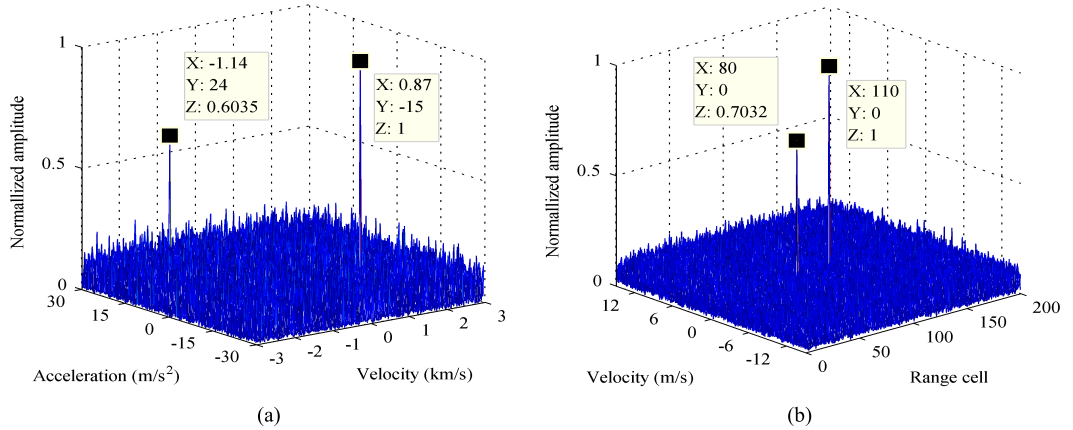

FIGURE 8. Verification of the proposed algorithm with the simulated radar data. (a) Target energy integration in the velocity and acceleration domain via the proposed algorithm. (b) Coherent energy integration after the RM and DFM compensations via the estimated motion parameters.

V. SIMULATION AND REAL DATA PROCESSING RESULT

In the last section, we demonstrate that the proposed algorithm can significantly reduce the computational complexity with an acceptable integration SNR gain loss In this section, we only aim to demonstrate the effectiveness of the proposed method for the maneuvering target detection via several experiments with the simulated and real measured radar data.

A. VERIFICATION WITH SIMULATED RADAR DATA

The radar parameters used in this simulation are the same as those in Section IV-B. Two targets are considered and their motion parameters are listed in Table 4. Targets' echoes are contaminated with the complex zero-mean white Gaussian noise and the SNR is also listed in Table 4. FIGURE. 8 shows the simulation results.

TABLE 4. Targets parameters.

Parameter	TA	TB
SNR (dB)	-32	-30
Range cell number	80th	110th
Radial velocity (m/s)	-1140	870
Radial acceleration (m/s2)	24	-15

As seen from FIGURE. 8(a), by using the proposed method, two peaks are accumulated in the velocity and acceleration domain. With the peak detection technique in FIGURE. 8(a), the radial velocities and accelerations of these two targets are estimated as (-1140 m/s, 24 m/s^2) and (870 m/s, -15 m/s^2), respectively. Thereafter, we compensate off the RMs and DFMs via the estimated motion parameters, and the coherent energy integration is realized in FIGURE. 8(b). Finally, by the CFAR detection technique, two targets can be easily detected.

B. VERIFICATION WITH REAL MEASURED RADAR DATA

In the following, the real measured data is used to verify the effectiveness of the proposed method. Table 5 gives the radar parameters. The data has a total of 1400 effective pulses and 300 range cells. We set both zoom factors ζ and ξ as 2 for the proposed method. Note that, in practice, we do not know whether the real measured radar data has problems of the RM and DFM or not. In this paper, we use the MTD and RFT to demonstrate that the used real measured radar data has problems of the RM and DFM. In addition, their comparisons can also demonstrate that the proposed method can work well in realistic applications. FIGURE. 9 shows the processing results of the MTD, RFT and the proposed algorithm. For the RFT, the scopes of the searching velocity and range cell are [-500 m/s, 500 m/s] and [50,150], respectively.

TABLE 5. Radar parameters.

Parameter	Value
Wave band	L
Bandwidth (MHz)	2
Sample frequency (MHz)	3.25
Pulse width (μs)	75
PRT (μs)	910

FIGURE. 9(a) shows echoes in the range-azimuth domain after the pulse compression. It is easily seen that the target moves across several range cells within the integration time.

By using the proposed algorithm, FIGURE. 9(b) gives the energy accumulation in the velocity and acceleration domain. Via the peak detection technique, the target's radial velocity and acceleration are estimated as -184.6 m/s and 0.2679 m/s^2, respectively. Thereafter, we compensate the RM and DFM with the estimated target's motion parameters, and FIGURE. 9(c) shows the coherent energy integration. To better show the focusing performance, a zoomed-in figure of the circled area is also presented in FIGURE. 9 (c). We can clearly observe that the proposed method achieves a good focusing performance in both the range and Doppler domains.

By performing the azimuth FFT on FIGURE. 9(a), we get the integration result of the MTD in FIGURE. 9(d).

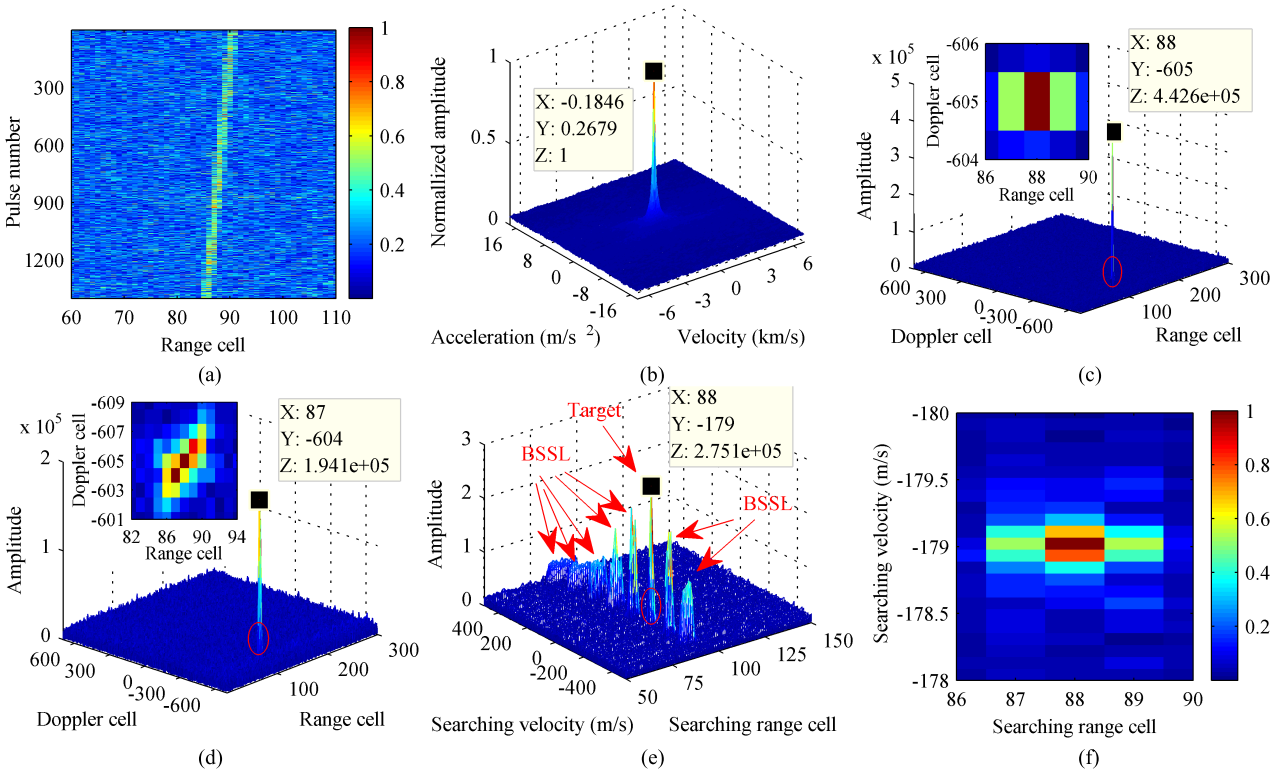

FIGURE 9. Real measured radar data processing results. (a) Pulse compression result. (b) Velocity and acceleration distribution via the proposed method. (c) Coherent integration results via the proposed method. (d)Integration result via MTD. (e) Integration results via RFT. (f) Zoomed-in plot of the circled area in (e).

The MTD has a bad focusing performance because of existences of the RM and DFM. According to the peak values of FIGUREs. 9(c) and (d), it is easy to obtain that the MTD suffers from about 7 dB integration SNR loss compared with the proposed method.

The integration result via the RFT is given in FIGURE. 9(e), and a zoomed-in image of the circled area is also shown in FIGURE. 9(f). As seen from FIGUREs. 9(e) and (f), the RFT outperforms the MTD and has about 3 dB integration SNR gain. This is because the RFT has the ability to eliminate the linear RM. However, compared with the proposed method, the RFT cannot eliminate the DFM and quadratic RM, and has about 4 dB integration SNR loss. Moreover, the RFT suffers from the BSSL effect as shown in FIGURE. 9(e), which may lead to false alarms [30].

The real data processing results clearly demonstrate that: 1) the RM and DFM significantly influence the coherent energy integration; 2) the proposed method can effectively accomplish the maneuvering target detection and parameters estimation

VI. CONCLUSIONS

In this paper, we have proposed a novel algorithm for maneuvering target detection and motion parameters estimation. Basing on mathematical analyses and numerical simulations, we demonstrate that, compared to several representative algorithms, the proposed algorithm can greatly reduce the computational complexity with an acceptable integration SNR gain loss. Further, we use the real measured radar data to verify the effectiveness of the proposed algorithm.

APPENDIX A

The echoes of the xth and yth target after pulse compression can be expressed as

$$\begin{aligned} \boldsymbol{S}_x(f_r, t_n) = {} & \rho_x \operatorname{rect}\left(\frac{f_r}{B}\right) \exp\left(-j4\pi \frac{v_{0x} t_n}{\lambda}\right) \\ & \times \exp\left(-j4\pi f_r \frac{v_x t_n}{c}\right) \\ & \times \exp\left[-j2\pi\left(1+\frac{f_r}{f_c}\right)\frac{2r_x + a_x t_n^2}{\lambda}\right] \end{aligned} \tag{26}$$

$$\begin{aligned} \boldsymbol{S}_y(f_r, t_n) = {} & \rho_y \operatorname{rect}\left(\frac{f_r}{B}\right) \exp\left(-j4\pi \frac{v_{0y} t_n}{\lambda}\right) \\ & \times \exp\left(-j4\pi f_r \frac{v_y t_n}{c}\right) \\ & \times \exp\left[-j2\pi\left(1+\frac{f_r}{f_c}\right)\frac{2r_y + a_y t_n^2}{\lambda}\right] \end{aligned} \tag{27}$$

The cross term will thus be

$$\begin{aligned} \boldsymbol{R}_{x,y}(f_r, t_n, \tau_n) = {} & \boldsymbol{S}_x(f_r, t_n + \tau_n)\, \boldsymbol{S}_y^*(f_r, t_n - \tau_n) \\ & + \boldsymbol{S}_y(f_r, t_n + \tau_n)\, \boldsymbol{S}_x^*(f_r, t_n - \tau_n) \end{aligned} \tag{28}$$

Let $\Delta r = r_x - r_y$, $\Delta v = v_x - v_y$, $\nabla v = \left(v_x + v_y\right)/2$, $\Delta v_0 = v_{0x} - v_{0y}$, $\nabla v_0 = \left(v_{0x} + v_{0y}\right)/2$, $\Delta a = a_x - a_y$, and $\nabla a = \left(a_x + a_y\right)/2$, and then performing the EKT on $\boldsymbol{R}_{x,y}\left(f_r, t_n, \tau_n\right)$, we get

$$\begin{aligned}\boldsymbol{P}_{x,y}\left(f_r, t_m, \tau_n\right) &= EKT\left[\boldsymbol{R}_{x,y}\left(f_r, t_n, \tau_n\right)\right] \\ &= \boldsymbol{P}_{1,x,y}\left(f_r, t_m, \tau_n\right) \\ &\quad \times \left[\boldsymbol{P}_{2,x,y}\left(f_r, t_m, \tau_n\right) + \boldsymbol{P}_{3,x,y}\left(f_r, t_m, \tau_n\right)\right]\end{aligned} \tag{29}$$

where

$$\begin{aligned}&\boldsymbol{P}_{1,x,y}\left(f_r, t_m, \tau_n\right) \\ &= \rho_x \rho_y \mathrm{rect}\left(\frac{f_r}{B}\right) \exp\left(-j8\pi \frac{\nabla v_0 \tau_n}{\lambda}\right) \\ &\quad \times \exp\left(-j8\pi \frac{\nabla v}{c} \tau_n f_r\right) \exp\left[-j2\pi \frac{4\nabla a t_m}{\xi\lambda}\right]\end{aligned} \tag{30}$$

$$\begin{aligned}&\boldsymbol{P}_{2,x,y}\left(f_r, t_m, \tau_n\right) \\ &= \exp\left[-j2\pi\left(1 + \frac{f_r}{f_c}\right)\frac{2\Delta r}{\lambda}\right] \\ &\quad \times \exp\left[-j4\pi\left(\frac{\Delta v_0}{\lambda} + f_r \frac{\Delta v}{c}\right)\frac{t_m}{\xi\left(1 + f_r/f_c\right)\tau_n}\right] \\ &\quad \times \exp\left[-j2\pi\left(1 + \frac{f_r}{f_c}\right)\frac{\Delta a \tau_n^2}{\lambda}\right] \\ &\quad \times \exp\left[-j2\pi \frac{\Delta a}{\lambda} \frac{t_m^2}{\xi^2\left(1 + f_r/f_c\right)\tau_n^2}\right]\end{aligned} \tag{31}$$

$$\begin{aligned}&\boldsymbol{P}_{3,x,y}\left(f_r, t_m, \tau_n\right) \\ &= \boldsymbol{P}_{2,x,y}^{\dagger}\left(f_r, t_m, \tau_n\right)\end{aligned} \tag{32}$$

Performing the FFT on (30) along t_m axis, we have

$$\begin{aligned}\boldsymbol{U}_{1,x,y}\left(f_r, f_{sd}, \tau_n\right) &= \rho_{u1} \mathrm{rect}\left(\frac{f_r}{B}\right) \exp\left(-j8\pi \frac{\nabla v_0 \tau_n}{\lambda}\right) \\ &\quad \times \exp\left(-j8\pi \frac{\nabla v}{c} \tau_n f_r\right) \delta \\ &\quad \times \left(f_{sd} + \frac{4\nabla a}{\lambda\xi}\right)\end{aligned} \tag{33}$$

Thereafter, applying the SIFT to (33) along the range frequency axis obtains

$$\begin{aligned}\boldsymbol{V}_{1,x,y}\left(t_s, f_{sd}, \tau_n\right) &= \rho_{v1} \mathrm{sinc}\left[B\left(t_s - \frac{4\nabla v}{\zeta c}\right)\right] \\ &\quad \times \delta\left(f_{sd} + \frac{4\nabla a}{\lambda\xi}\right) \exp\left(-j8\pi \frac{\nabla v_0 \tau_n}{\lambda}\right)\end{aligned} \tag{34}$$

Finally, Taking the FFT of $\boldsymbol{V}_{1,x,y}\left(t_s, f_{sd}, \tau_n\right)$ with respect to τ_n, we get

$$\begin{aligned}\boldsymbol{Z}_{1,x,y}\left(t_s, f_{sd}, f_{pd}\right) &= \rho_{z1} \mathrm{sinc}\left[B\left(t_s - \frac{4\nabla v}{\zeta c}\right)\right] \\ &\quad \times \delta\left(f_{sd} + \frac{4\nabla a}{\lambda\xi}\right) \delta\left(f_{pd} + \frac{4\nabla v_0}{\lambda}\right)\end{aligned} \tag{35}$$

In what follows, we will analyzed the cross terms in three cases.

Case 1: $\Delta a = 0$ and $\Delta v \neq 0$.

The equation (31) will be of the form

$$\begin{aligned}&\boldsymbol{P}_{2,x,y}\left(f_r, t_m, \tau_n\right) \\ &= \exp\left[-j2\pi\left(1 + \frac{f_r}{f_c}\right)\frac{2\Delta r}{\lambda}\right] \\ &\quad \times \exp\left[-j4\pi\left(\frac{\Delta v_0}{\lambda} + f_r \frac{\Delta v}{c}\right)\frac{t_m}{\xi\left(1 + f_r/f_c\right)\tau_n}\right]\end{aligned} \tag{36}$$

Performing the FFT on (36) with respect to t_m obtains

$$\begin{aligned}\boldsymbol{U}_{2,x,y}\left(f_r, f_{sd}, \tau_n\right) &= \rho_{u2} \exp\left[-j2\pi\left(1 + \frac{f_r}{f_c}\right)\frac{2\Delta r}{\lambda}\right] \\ &\quad \times \delta\left(f_{sd} + \frac{2\left(\Delta v_0/\lambda + f_r \Delta v/c\right)}{\xi\left(1 + f_r/f_c\right)\tau_n}\right)\end{aligned} \tag{37}$$

Similarly, we have

$$\begin{aligned}\boldsymbol{U}_{3,x,y}\left(f_r, f_{sd}, \tau_n\right) &= \rho_{u3} \exp\left[j2\pi\left(1 + \frac{f_r}{f_c}\right)\frac{2\Delta r}{\lambda}\right] \\ &\quad \times \delta\left(f_{sd} - \frac{2\left(\Delta v_0/\lambda + f_r \Delta v/c\right)}{\xi\left(1 + f_r/f_c\right)\tau_n}\right)\end{aligned} \tag{38}$$

According to the convolution theorem, we have

$$\begin{aligned}&\boldsymbol{U}_{x,y}\left(f_r, f_{sd}, \tau_n\right) \\ &= conv_{f_{sd}}\left\{\boldsymbol{U}_{1,x,y}\left(f_r, f_{sd}, \tau_n\right), \right. \\ &\quad \left. \times \left[\boldsymbol{U}_{2,x,y}\left(f_r, f_{sd}, \tau_n\right) + \boldsymbol{U}_{3,x,y}\left(f_r, f_{sd}, \tau_n\right)\right]\right\} \\ &= \rho_{u1}\rho_{u2} \mathrm{rect}\left(\frac{f_r}{B}\right) \delta\left[f_{sd} + \frac{2\left(\Delta v_0/\lambda + f_r \Delta v/c\right)}{\xi\left(1 + f_r/f_c\right)\tau_n} + \frac{4\nabla a}{\lambda\xi}\right] \\ &\quad \times \exp\left[-j2\pi\left(1 + \frac{f_r}{f_c}\right)\frac{2\Delta r}{\lambda}\right] \exp\left(-j8\pi \frac{\nabla v_0 \tau_n}{\lambda}\right) \\ &\quad \times \exp\left(-j8\pi \frac{\nabla v}{c} \tau_n f_r\right) \\ &\quad + \rho_{u1}\rho_{u3} \mathrm{rect}\left(\frac{f_r}{B}\right) \delta\left[f_{sd} - \frac{2\left(\Delta v_0/\lambda + f_r \Delta v/c\right)}{\xi\left(1 + f_r/f_c\right)\tau_n} + \frac{4\nabla a}{\lambda\xi}\right] \\ &\quad \times \exp\left[j2\pi\left(1 + \frac{f_r}{f_c}\right)\frac{2\Delta r}{\lambda}\right] \exp\left(-j8\pi \frac{\nabla v_0 \tau_n}{\lambda}\right) \\ &\quad \times \exp\left(-j8\pi \frac{\nabla v}{c} \tau_n f_r\right)\end{aligned} \tag{39}$$

where $conv_{f_{sd}}\{A, B\}$ denotes the convolution operation in the f_{sd} domain. It can be seen from (39) that the cross term could not be accumulated by the further operations (SIFT along the range frequency axis and FFT along the lag time axis).

Case 2: $\Delta a = 0$, $\Delta v = 0$, and $\nabla r \neq 0$.

(37) can be rewritten as

$$\begin{aligned}\boldsymbol{U}_{2,x,y}\left(f_r, f_{sd}, \tau_n\right) &= \exp\left(-j2\pi \frac{2\Delta r}{\lambda}\right) \\ &\quad \times \exp\left(-j2\pi f_r \frac{2\Delta r}{c}\right) \delta\left(f_{sd}\right)\end{aligned} \tag{40}$$

Performing the SIFT on (40)

$$\begin{aligned}\boldsymbol{V}_{2,x,y}(t_s,f_{sd},\tau_n) &= SIFT_{f_r}\left[\boldsymbol{U}_{2,x,y}(f_r,f_{sd},\tau_n)\right]\\ &= \exp\left(-j2\pi\frac{2\Delta r}{\lambda}\right)\delta\left(t_s-\frac{2\Delta r}{\zeta c\tau_n}\right)\delta(f_{sd})\end{aligned} \tag{41}$$

In the following, we discuss two cases according to the value of t_s.

Case 2.1: $t_s = 0$.

With $\Delta r \neq 0$, (41) will be zeros, so we have

$$\boldsymbol{V}_{2,x,y}(t_s,f_{sd},\tau_n) = \boldsymbol{V}_{3,x,y}(t_s,f_{sd},\tau_n) = 0 \tag{42}$$

Therefore, the cross term will be zero.

Case 2.2: $t_s \neq 0$

According to the composition property of the delta function, i.e.,

$$\delta[f(t)] = \sum_{i=1}^{N}\frac{1}{|f'(t_i)|}\delta(t-t_i) \tag{43}$$

where $f'(\cdot)$ denotes the first derivative, t_i denotes the ith root of $f(t) = 0$.

Thus, (41) can be rewritten as

$$\begin{aligned}\boldsymbol{V}_{2,x,y}(t_s,f_{sd},\tau_n) &= \frac{2\Delta r}{\zeta c t_s^2}\delta\left(\tau_n-\frac{2\Delta r}{\zeta c t_s}\right)\\ &\quad\times\exp\left(-j2\pi\frac{2\Delta r}{\lambda}\right)\delta(f_{sd})\end{aligned} \tag{44}$$

Applying the FFT to (44) along the lag time axis, we have

$$\begin{aligned}\boldsymbol{Z}_{2,x,y}(t_s,f_{sd},f_{pd}) &= \frac{2\Delta r}{\zeta c t_s^2}\exp\left(-j2\pi\frac{2\Delta r}{\lambda}\right)\\ &\quad\times\exp\left(-j2\pi f_{pd}\frac{2\Delta r}{\zeta c t_s}\right)\delta(f_{sd})\end{aligned} \tag{45}$$

Similarly,

$$\begin{aligned}\boldsymbol{Z}_{3,x,y}(t_s,f_{sd},f_{pd}) &= \frac{2\Delta r}{\zeta c t_s^2}\exp\left(j2\pi\frac{2\Delta r}{\lambda}\right)\\ &\quad\times\exp\left(j2\pi f_{pd}\frac{2\Delta r}{\zeta c t_s}\right)\delta(f_{sd})\end{aligned} \tag{46}$$

Therefore,

$$\begin{aligned}&\boldsymbol{Z}_{2,x,y}(t_s,f_{sd},f_{pd})+\boldsymbol{Z}_{3,x,y}(t_s,f_{sd},f_{pd})\\ &\quad=\frac{2\Delta r}{\zeta c t_s^2}\cos\left[2\pi\left(\frac{2\Delta r}{\lambda}+f_{pd}\frac{2\Delta r}{\zeta c t_s}\right)\right]\delta(f_{sd})\end{aligned} \tag{47}$$

Case 2.2.1: $t_s = \frac{4\nabla v}{\zeta c}$

By substitution $t_s = \frac{4\nabla v}{\zeta c}$ into (47), we have

$$\begin{aligned}&\boldsymbol{Z}_{2,x,y}(t_s,f_{sd},f_{pd})+\boldsymbol{Z}_{3,x,y}(t_s,f_{sd},f_{pd})\\ &\quad=\frac{\zeta c\Delta r}{8(\nabla v)^2}\cos\left[2\pi\left(\frac{2\Delta r}{\lambda}+f_{pd}\frac{\Delta r}{2\nabla v}\right)\right]\delta(f_{sd})\end{aligned} \tag{48}$$

According to the convolution theorem, we have

$$\begin{aligned}&\boldsymbol{Z}_{x,y}(t_s,f_{sd},f_{pd})\\ &\quad=conv_{t_s,f_{sd},f_{pd}}\left\{\boldsymbol{Z}_{1,x,y}(t_s,f_{sd},f_{pd}),\right.\\ &\qquad\left.\left[\boldsymbol{Z}_{2,x,y}(t_s,f_{sd},f_{pd})+\boldsymbol{Z}_{3,x,y}(t_s,f_{sd},f_{pd})\right]\right\}\\ &\quad=\frac{\zeta c\Delta r}{8(\nabla v)^2}\mathrm{sinc}\left[B\left(t_s-\frac{4\nabla v}{\zeta c}\right)\right]\delta\left(f_{sd}+\frac{4\nabla a}{\lambda\xi}\right)\\ &\qquad\times\cos\left\{2\pi\left[\frac{2\Delta r}{\lambda}+\left(f_{pd}+\frac{4\nabla v_0}{\lambda}\right)\frac{\Delta r}{2\nabla v}\right]\right\}\end{aligned} \tag{49}$$

Observation of (49) shows that the cross term energy can be accumulated in the t_s and f_{sd} domains. However, the cross term energy still spreads in the f_{sd} domain, which indicates that the cross term cannot be accumulated in this case.

Case 2.2.2: $t_s \neq \frac{4\nabla v}{\zeta c}$

We have

$$\begin{aligned}&\boldsymbol{Z}_{x,y}(t_s,f_{sd},f_{pd})\\ &=conv_{t_s,f_{sd},f_{pd}}\left\{\boldsymbol{Z}_{1,x,y}(t_s,f_{sd},f_{pd})\right.\\ &\qquad\left.\left[\boldsymbol{Z}_{2,x,y}(t_s,f_{sd},f_{pd})+\boldsymbol{Z}_{3,x,y}(t_s,f_{sd},f_{pd})\right]\right\}\\ &=\frac{2\Delta r}{\zeta c\left[t_s-4\nabla v/(\zeta c)\right]^2}\delta\left(f_{sd}+\frac{4\nabla a}{\lambda\xi}\right)\\ &\qquad\times\cos\left\{2\pi\left[\frac{2\Delta r}{\lambda}+\left(f_{pd}+\frac{4\nabla v_0}{\lambda}\right)\frac{2\Delta r}{\zeta c\left(t_s-4\nabla v/(\zeta c)\right)}\right]\right\}\end{aligned} \tag{50}$$

As can be seen from (50), the cross term energy cannot be focused in t_s and f_{pd} domain.

Case 3: $\Delta a \neq 0$.

It is obvious that $\boldsymbol{P}_{2,x,y}(f_r,t_m,\tau_n)$ in (31) and $\boldsymbol{P}_{3,x,y}(f_r,t_m,\tau_n)$ in (32) cannot be accumulated by the FFT operation along t_m axis, so the cross term cannot be accumulated.

The above analyses shows that the cross term cannot accumulate as the auto term.

APPENDIX B

According to (40), $\boldsymbol{U}_{A,B}(f_r,f_{sd},\tau_n)$ satisfies

$$\begin{aligned}&\left|\boldsymbol{U}_{A,B}(f_r,f_{sd},\tau_n)\right|\\ &\quad=\delta\left[f_{sd}+\frac{4\nabla a_{A,B}}{\lambda\xi}-\frac{2\left(\Delta v_{0,A,B}/\lambda+f_r\Delta v_{A,B}/c\right)}{\xi\left(1+f_r/f_c\right)\tau_n}\right]\\ &\qquad+\delta\left[f_{sd}+\frac{4\nabla a_{A,B}}{\lambda\xi}+\frac{2\left(\Delta v_{0,A,B}/\lambda+f_r\Delta v_{A,B}/c\right)}{\xi\left(1+f_r/f_c\right)\tau_n}\right]\end{aligned} \tag{51}$$

Substituting $\xi = 4, f_r = 5$ MHz, $v_{0A} = -21.6$ m/s, $v_{0B} = -28.8$ m/s, $\Delta v_{0,A,B} = 7.2$m/s, $\Delta v_{A,B} = -300$ m/s, and $\nabla a_{A,B} = 45$ m/s^2 into (51), we have

$$\begin{aligned}\left|\boldsymbol{U}_{A,B}(5\ MHz,f_{sd},\tau_n)\right| &= \delta\left(f_{sd}+150-\frac{1900}{201\tau_n}\right)\\ &\quad+\delta\left(f_{sd}+150+\frac{1900}{201\tau_n}\right)\end{aligned} \tag{52}$$

So the cross term generated by T_A and T_B distributes along $f_{sd} = -150 + 1900/(201\tau_n)$ Hz and $f_{sd} = -150 - 1900/(201\tau_n)$ Hz in $\left|\boldsymbol{U}_{A,B}\left(5\ MHz, f_{sd}, \tau_n\right)\right|$.

T_B and T_C have the same radial velocity and acceleration, so the cross term generated by T_A and T_C peaks along the same curves as the cross term generated by T_A and T_B.

According to convolution theorem, the cross term generated by T_B and T_C satisfies

$$\left|\boldsymbol{U}_{B,C}\left(f_r, f_{sd}, \tau_n\right)\right| = \delta\left(f_{sd} + \frac{4\nabla a_{B,C}}{\lambda\xi}\right) \tag{53}$$

Thus, the cross term generated by T_B and T_C distributes along $f_{sd} = -150$ Hz in $\left|\boldsymbol{U}_{B,C}\left(5\ MHz, f_{sd}, \tau_n\right)\right|$.

$\boldsymbol{V}_{B,C}\left(t_s, f_{sd}, \tau_n\right)$ can be expressed as

$$\begin{aligned}\boldsymbol{V}_{B,C}\left(t_s, f_{sd}, \tau_n\right) = conv_{t_s, f_{sd}}\{&\boldsymbol{V}_{1,B,C}\left(t_s, f_{sd}, \tau_n\right), \\ &\times \left[\boldsymbol{V}_{2,B,C}\left(t_s, f_{sd}, \tau_n\right) + \boldsymbol{V}_{3,B,C}\left(t_s, f_{sd}, \tau_n\right)\right]\}\end{aligned} \tag{54}$$

where $conv_{t_s, f_{sd}}\{A, B\}$ denotes the convolution operation in t_s and f_{sd} the domains.

After substituting (34) and (41) into (54), the cross terms generated by T_B and T_C satisfies

$$\begin{aligned}&\left|\boldsymbol{V}_{B,C}\left(t_s, f_{sd}, \tau_n\right)\right| \\ &= \delta\left(t_s - \frac{4\nabla v_{B,C}}{\zeta c} - \frac{2\Delta r_{B,C}}{\zeta c\tau_n}\right)\delta\left(f_{sd} + \frac{4\nabla a_{B,C}}{\lambda\xi}\right) \\ &\quad + \delta\left(t_s - \frac{4\nabla v_{B,C}}{\zeta c} + \frac{2\Delta r_{B,C}}{\zeta c\tau_n}\right)\delta\left(f_{sd} + \frac{4\nabla a_{B,C}}{\lambda\xi}\right)\end{aligned} \tag{55}$$

Substituting $\xi = 4$, $\zeta = 2$, $\nabla v_{B,C} = 1200$ m/s, $\Delta r_{B,C} = 300$ m, and $\nabla a_{B,C} = 45$ m/s ^{2} into (55), we get

$$\begin{aligned}&\left|\boldsymbol{V}_{B,C}\left(t_s, f_{sd}, \tau_n\right)\right| \\ &= \delta\left(t_s - 8\times 10^{-6} - \frac{10^{-6}}{\tau_n}\right)\delta\left(f_{sd} + 150\right) \\ &\quad + \delta\left(t_s - 8\times 10^{-6} + \frac{10^{-6}}{\tau_n}\right)\delta\left(f_{sd} + 150\right)\end{aligned} \tag{56}$$

Therefore, the cross term peaks along $t_s = 8 + 1/\tau_n\mu$s, and $t_s = 8 - 1/\tau_n\mu$s in $\left|\boldsymbol{V}_{B,C}\left(t_s, -150Hz, \tau_n\right)\right|$.

REFERENCES

[1] M. I. Skolnik, *Radar Handbook*. New York, NY, USA: McGraw-Hill, 1990.

[2] B. D. Carlson, E. D. Evans, and S. L. Wilson, "Search radar detection and track with the Hough transform. Part I. System concept," *IEEE Trans. Aerosp. Electron. Syst.*, vol. 30, no. 1, pp. 102–108, Jan. 1994.

[3] E. Grossi *et al.*, "A new look at the radar detection problem," *IEEE Trans. Signal. Process.*, vol. 64, no. 22, pp. 5835–5847, Nov. 2016.

[4] W. D. Wirth, "Long term coherent integration for a floodlight radar," in *Proc. IEEE Int. Radar Conf.*, May 1995, pp. 698–703.

[5] J. Xu, J. Yu, Y.-N. Peng, and X.-G. Xia, "Long-time coherent integration for radar target detection base on Radon-Fourier transform," in *Proc. IEEE Radar Conf.*, May 2010, pp. 432–436.

[6] R. Tao, N. Zhang, and Y. Wang, "Analysing and compensating the effects of range and Doppler frequency migrations in linear frequency modulation pulse compression radar," *IET Radar, Sonar Navigat.*, vol. 5, no. 1, pp. 12–22, Jan. 2011.

[7] S.-S. Zhang, T. Zeng, T. Long, and H.-P. Yuan, "Dim target detection based on keystone transform," in *Proc. IEEE Int. Radar Conf.*, May 2005, pp. 889–894.

[8] R. P. Perry, R. C. DiPietro, and R. L. Fante, "Coherent integration with range migration using keystone formatting," in *Proc. IEEE Radar Conf.*, Apr. 2007, pp. 863–868.

[9] D. Kirkland, "Imaging moving targets using the second-order keystone transform," *IET Radar, Sonar Navigat.*, vol. 5, no. 8, pp. 902–910, Oct. 2011.

[10] K. M. Scott, W. C. Barott, and B. Himed, "The keystone transform: Practical limits and extension to second order corrections," in *Proc. IEEE Radar Conf.*, May 2015, pp. 1264–1269.

[11] G. Li, X. G. Xia, and Y. N. Peng, "Doppler keystone transform: An approach suitable for parallel implementation of SAR moving target imaging," *IEEE Geosci. Remote Sens. Lett.*, vol. 5, no. 4, pp. 573–577, Oct. 2008.

[12] L. Kong, X. Li, G. Cui, W. Yi, and Y. Yang, "Coherent integration algorithm for a maneuvering target with high-order range migration," *IEEE Trans. Signal Process.*, vol. 63, no. 17, pp. 4474–4486, Sep. 2015.

[13] P. Huang, G. Liao, Z. Yang, X. G. Xia, J. Ma, and X. Zhang, "A fast SAR imaging method for ground moving target using a second-order WVD transform," *IEEE Trans. Geosci. Remote Sens.*, vol. 54, no. 4, pp. 1940–1956, Apr. 2016.

[14] J. Xu, J. Yu, Y.-N. Peng, and X.-G. Xia, "Radon-Fourier transform for radar target detection, I: Generalized Doppler filter bank," *IEEE Trans. Aerosp. Electron. Syst.*, vol. 47, no. 2, pp. 1186–1202, Apr. 2011.

[15] J. Xu, X.-G. Xia, S.-B. Peng, J. Yu, Y.-N. Peng, and L.-C. Qian, "Radar maneuvering target motion estimation based on generalized radon-Fourier transform," *IEEE Trans. Signal Process.*, vol. 60, no. 12, pp. 6190–6201, Dec. 2012.

[16] X. Chen, J. Guan, N. Liu, and Y. He, "Maneuvering target detection via Radon-fractional Fourier transform-based long-time coherent integration," *IEEE Trans. Signal Process.*, vol. 62, no. 4, pp. 939–953, Feb. 2014.

[17] X. Li, G. Cui, W. Yi, and L. Kong, "Coherent integration for maneuvering target detection based on Radon-Lv's distribution," *IEEE Signal Process. Lett.*, vol. 22, no. 9, pp. 1467–1471, Sep. 2015.

[18] X. Chen, J. Guan, Y. Huang, N. Liu, and Y. He, "Radon-linear canonical ambiguity function-based detection and estimation method for marine target with micromotion," *IEEE Trans. Geosci. Remote Sens.*, vol. 53, no. 4, pp. 2225–2240, Apr. 2015.

[19] Y. Li, M. Xing, J. Su, Y. Quan, and Z. Bao, "A new algorithm of ISAR imaging for maneuvering targets with low SNR," *IEEE Trans. Aerosp. Electron. Syst.*, vol. 49, no. 1, pp. 543–557, Jan. 2013.

[20] X. Li, G. Cui, W. Yi, and L. Kong, "A fast maneuvering target motion parameters estimation algorithm based on ACCF," *IEEE Signal Process. Lett.*, vol. 22, no. 3, pp. 270–274, Mar. 2015.

[21] X. Li, G. Cui, L. Kong, and W. Yi, "Fast non-searching method for maneuvering target detection and motion parameters estimation," *IEEE Trans. Signal Process.*, vol. 64, no. 9, pp. 2232–2244, May 2016.

[22] J. Zheng, T. Su, W. Zhu, X. He, and Q. H. Liu, "Radar high-speed target detection based on the scaled inverse Fourier transform," *IEEE J. Sel. Topics Appl. Earth Observ. Remote Sens.*, vol. 8, no. 3, pp. 1108–1119, Mar. 2015.

[23] J. Zheng, T. Su, H. Liu, G. Liao, Z. Liu, and Q. H. Liu, "Radar high-speed target detection based on the frequency-domain deramp-keystone transform," *IEEE J. Sel. Topics Appl. Earth Observ. Remote Sens.*, vol. 9, no. 1, pp. 285–294, Jan. 2016.

[24] L. B. Almeida, "The fractional Fourier transform and time-frequency representations," *IEEE Trans. Signal Process.*, vol. 42, no. 11, pp. 3084–3091, Nov. 1994.

[25] X. Lv, G. Bi, C. Wan, and M. Xing, "Lv's distribution: Principle, implementation, properties, and performance," *IEEE Trans. Signal Process.*, vol. 59, no. 8, pp. 3576–3591, Aug. 2011.

[26] S. Luo, G. Bi, X. Lv, and F. Hu, "Performance analysis on Lv distribution and its applications," *Digit. Signal Process.*, vol. 23, pp. 797–807, 2013.

[27] J. Tian, W. Cui, and S. Wu, "A novel method for parameter estimation of space moving targets," *IEEE Geosci. Remote Sens. Lett.*, vol. 11, no. 2, pp. 389–393, Feb. 2014.

[28] X. Rao, H. Tao, J. Su, J. Xie, and X. Zhang, "Detection of constant radial acceleration weak target via IAR-FRFT," *IEEE Trans. Aerosp. Electron. Syst.*, vol. 51, no. 4, pp. 3242–3253, Oct. 2016.

[29] X. Bai, R. Tao, Z. Wang, and Y. Wang, "ISAR imaging of a ship target based on parameter estimation of multicomponent quadratic frequency-modulated signals," *IEEE Trans. Geosci. Remote Sens.*, vol. 52, no. 2, pp. 1418–1429, Feb. 2014.

[30] J. Xu, J. Yu, Y.-N. Peng, and X.-G. Xia, "Radon-Fourier transform for radar target detection (II): Blind speed sidelobe suppression," *IEEE Trans. Aerosp. Electron. Syst.*, vol. 47, no. 4, pp. 2473–2489, Oct. 2011.
[31] X. Li, L. Kong, G. Cui, and W. Yi, "CLEAN-based coherent integration method for high-speed multi-targets detection," *IET Radar Sonar Navigat.*, vol. 10, no. 9, pp. 1671–1682, 2017.
[32] J. Zheng, T. Su, W. Zhu, L. Zhang, Z. Liu, and Q. H. Liu, "ISAR imaging of nonuniformly rotating target based on a fast parameter estimation algorithm of cubic phase signal," *IEEE Trans. Geosci. Remote Sens.*, vol. 53, no. 9, pp. 4727–4740, Sep. 2015.

JIBIN ZHENG (M'17) received the B.S. degree in electronic information science and technology from Shandong Normal University, Jinan, China, in 2009, and the Ph.D. degree in signal and information processing from Xidian University, Xi'an, China, in 2015.

From 2012 to 2014, he worked as a Visiting Ph.D. at the Department of Electrical Engineering, Duke University, Durham, NC, USA, under the financial support from the China Scholarship Council. Since 2015, he has been a Faculty Member with the National Laboratory of Radar Signal Processing, Xidian University, where he is currently an Associate Professor. His research interests include synthetic aperture radar (SAR) and inverse SAR signal processing, cognitive radar, time–frequency analysis, sparse Bayes learning, and KA-clutter suppression.

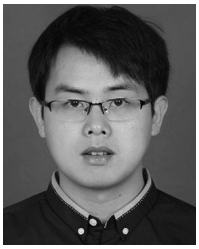

JIANCHENG ZHANG was born in Jiangxi, China, in 1989. He received the B.S. degree in measurement and control technology and instrumentation from Xidian University, Xi'an, China, in 2011, where he is currently pursuing the Ph.D. degree with the National Laboratory of Radar Signal Processing.

His research interests include maneuvering target detection, parameter estimation, and time–frequency analysis.

SHUWEN XU (M'10) received the B.Eng. and Ph.D. degrees from Xidian University, Xi'an, China, in 2006 and 2011, respectively, both in electronic engineering. Then, he worked at the School of Electronic Engineering, Xidian University.

He is currently an Associate Professor with Xidian University, and also a Visiting Professor with McMaster University, Canada. His research interests are in the fields of target detection, statistical learning theory, and SAR image processing.

HONGWEI LIU (M'04) received the M.Eng. and Ph.D. degrees in electronic engineering from Xidian University, Xi'an, China, in 1995 and 1999, respectively.

From 2001 to 2002, he was a Visiting Scholar with the Department of Electrical and Computer Engineering, Duke University, Durham, NC, USA. He is currently a Professor with the National Laboratory of Radar Signal Processing, Xidian University, and the Director of the National Laboratory of Radar Signal Processing. His research interests include radar signal processing, radar automatic target recognition, adaptive signal processing, and cognitive radar.

QING HUO LIU (S'88–M'89–SM'94–F'05) received the B.S. and M.S. degrees in physics from Xiamen University, Fujian, China, in 1983 and 1986, respectively, and the Ph.D. degree in electrical engineering from the University of Illinois at Urbana–Champaign in 1989.

He was with the Electromagnetics Laboratory, University of Illinois at Urbana–Champaign, as a Research Assistant, from 1986 to 1988, and as a Post-Doctoral Research Associate from 1989 to 1990. He was a Research Scientist and the Program Leader with the Schlumberger-Doll Research Center, Cambridge, MA, USA, from 1990 to 1995. From 1996 to 1999, he was an Associate Professor with New Mexico State University, Las Cruces, NM, USA. Since 1999, he has been with Duke University, Durham, NC, USA, where he is currently a Professor of electrical and computer engineering. He is also a Visiting Professor at the University of Electronic Science and Technology of China. His research interests include computational electromagnetics and acoustics, inverse problems, geophysical subsurface sensing, biomedical imaging, electronic packaging, and the simulation of photonic and nano devices.